

Optimized CT-MR Neurological Image Fusion Framework using Biologically Inspired Spiking Neural Model in Hybrid ℓ_1 - ℓ_0 Layer Decomposition Domain

Abstract

Medical image fusion plays an important role in the clinical diagnosis of several critical neurological diseases by merging complementary information available in multimodal images. In this paper, a novel CT-MR neurological image fusion framework is proposed using an optimized biologically inspired feedforward neural model in two-scale hybrid $\ell_1 - \ell_0$ decomposition domain using gray wolf optimization to preserve the structural as well as texture information present in source CT and MR images. Initially, the source images are subjected to two-scale $\ell_1 - \ell_0$ decomposition with optimized parameters, giving a scale-1 detail layer, a scale-2 detail layer and a scale-2 base layer. Two detail layers at scale-1 and 2 are fused using an optimized biologically inspired neural model and weighted average scheme based on local energy and modified spatial frequency to maximize the preservation of edges and local textures, respectively, while the scale-2 base layer gets fused using choose max rule to preserve the background information. To optimize the hyper-parameters of hybrid $\ell_1 - \ell_0$ decomposition and biologically inspired neural model, a fitness function is evaluated based on spatial frequency and edge index of the resultant fused image obtained by adding all the fused components. The fusion performance is analyzed by conducting extensive experiments on different CT-MR neurological images. Experimental results indicate that the proposed method provides better-fused images and outperforms the other state-of-the-art fusion methods in both visual and quantitative assessments.

Keywords: CT, MR, Image fusion, Hybrid $\ell_1 - \ell_0$ layer decomposition, Biologically inspired spiking neural model

1. Introduction

Brain is the most complex organ which controls various physiological functions of the body. Neural activities of the brain are also responsible for

steering a person's emotions which ultimately drive his/her social behavior. Even an acute physical injury or minor abnormality in its function can lead to catastrophic damages. Hence, there is a continuous need for advancements in tools and techniques which help to visualize and analyze different brain structures more meticulously. There are several medical imaging modalities as X-ray, ultra Sound (US), Computed Tomography (CT), Magnetic Resonance (MR), etc. which can provide different kind of information (anatomic, functional, etc.) of the body part being imaged. However, no single medical image modality can provide complete and comprehensive diagnostic information, especially in critical diseases. For example, CT is preferred to image hard-tissue structures like bones and provides an accurate diagnosis of skull injuries, brain calcification, etc., while MR is considered better to image soft tissues and provides excellent anatomical details of various brain lesions [1]. Therefore, it is necessary to find out the correlation between different imaging modalities to provide significant information which is very time consuming for clinicians and costly for an individual. Therefore, there is a need to develop a unique solution that is used to improve the effectiveness of analyzing methods to determine the level of severity associated with the disease. The proposed work is focused on the problem of analyzing the multi-modal medical images. The fusion of the complementary anatomical information provided by CT and MR modalities results in more localized and factual clinical interpretations. Hence, CT-MR medical image fusion can be regarded as a high-value tool for clinicians and radiologists to infer the causes of different neurological anomalies and may assist them to come up with a more accurate and reliable diagnosis, especially in critical neurological diseases.

In past years, several image fusion methods have been reported in the literature which can be categorized into spatial domain and transform domain [2]. In spatial domain fusion methods, source pixels are fused directly based on their intensities or some regional activities, while in transform domain methods, firstly reference images are decomposed using multi-scale transformation and then the transform coefficients at each scales are fused using different fusion rules based on their values or activity levels. Though spatial domain image fusion methods have an advantage of less computational complexity, its results are limited to poor contrast, artifacts, and blurring effects in the fused image. Multiscale transform-based approaches can extract both the spatial and spectral information and hence provide better localization to spatial structures present in the source images. In this context, a wide range of multiscale transform-based fusion approaches are presented in the literature [3]. Pyramid decomposition-based methods outperform spatial do-

main fusion, however, they suffer from blocking effects because they are not able to offer directional selectivity [4]. Discrete wavelet transform (DWT)-based fusion provides direction selectivity and captures 1-dimensional point singularities resulting in reduced blocking artifacts. However, artifacts are still introduced in the regions of line or curve singularities [5]. Furthermore, different decompositions such as curvelet (CVT) [6], contourlet (CT) [7] and shearlet transform (ST) [8]-based methods have been reported to reflect higher-order singularities and to provide an improved fusion performance. However, subsequent subsampling at each scale makes it shift variant. The shift-invariance property of nonsubsampling contourlet transform (NSCT) [9, 10, 11], nonsubsampling shearlet transform (NSST) [12, 13, 14] and stationary wavelet transforms (SWT) [15, 16] overcomes the problem of shift-invariance and offers better fusion performance in terms of the edge preservation. Moreover, to preserve small edges present in the source images, the number of decomposition levels has to be increased which further increases the computational complexity.

The main motivation of the proposed work is to preserve the energy of the source images and provides perceptually appealing fused images. To achieve this, it is important to develop such fusion methods that are capable to preserve small diagnostic detail and edges as much as possible by enhancing the visualization of fused images. Hence, an edge-preserving decomposition named as hybrid $\ell_1 - \ell_0$ layer decomposition (HLD) model [17] having two ℓ_1 and ℓ_0 sparsity terms for detail and base layer, individually is utilized in the proposed approach to capture sharp edges and weak structural details, respectively. However, the fusion performance largely depends on the regularization parameters ($\lambda_1, \lambda_2, \lambda_3$) which control the degree of smoothness of base and detail layers. Conventionally, these values are manually chosen based on successive experiments at a regular interval or hit and trial method [17, 18] which may not lead to optimal performance. To overcome the limitation of manual selection of hyper-parameters, gray wolf optimization technique (GWO) [19] is utilized in the presented work to optimize $\lambda_1, \lambda_2, \lambda_3$ regularization parameters of $\ell_1 - \ell_0$ HLD model.

Alongwith the proper selection of the decomposition method, it is very important to devise an intelligent fusion rule for detail and base layers, individually to conserve the spatial information and edge information present in the base and detail layers, respectively. Normally, base layer coefficients carry most of the energy and textural details of the source images. Simple averaging fusion rule results in significant loss of texture information and contrast [20]. Weighted average based on local energy, Laplacian energy [10], and variance [21], etc. have shown better performance with lesser com-

putational cost. Moreover, detail layer coefficients carry structural details and edge information available in the source images. To preserve maximum structural information, some activity level measures such as local log Gabor energy [22, 23], directive contrast [24], phase congruency and sharpness [10], etc are utilized by choose max rule. Moreover, biologically-inspired spiking feedforward neural network (BISFNN) such as pulse coupled neural (PCNN) model and its variants are extensively utilized in the formulation of image fusion algorithm because of its ability to extract features consistent with human vision [2, 5, 12, 13, 25, 26]. In these approaches, each neuron is subjected to local activities of input coefficients such as intensity, regional energy, a novel modified spatial frequency, novel sum modified Laplacian, etc. [2, 5]. However, the major limitation of the conventional BISFNN model is the optimal selection of its free parameters (α_L , α_T , β , V_L , V_T) which depend on the nature and texture of the input source images. In the past years, the selection of all free parameters was done based on successive experiments on a regular interval (or hit and trial approach) [5, 12, 27]. To overcome the limitation of manual selection, some fusion methods are developed based on the adaptive selection of few free parameters using local contrast, entropy, directional gradient, saliency, local visibility and intensity of pixels or coefficients [23, 25, 28, 29, 30, 31, 32]. They showed improved fusion performance, however, successive trials based parameter selection is involved in those approaches. Besides the PCNN based fusion methods, sparse representation and deep learning-based fusion approaches have also been presented recently in [33, 34, 35, 36, 37, 38] and showed better preservation of textures, but involve a large number of training samples and computations.

With the consideration of the aforementioned discussion, an optimized CT-MR neurological image fusion framework is presented in this paper by optimizing the free parameters of $\ell_1-\ell_0$ HLD model and BISFNN model using the gray wolf optimization (GWO) technique.

Firstly, source CT and MR-T2 neurological images are subjected to two-scale $\ell_1-\ell_0$ HLD decomposition to extract the structural and textural components from source images and also to reduce the effect of noise and artifacts simultaneously. To extract the structural information present in the source images, detail layers at scale-1 are fused using optimized BISFNN based on firing time, whereas the detail layer at scale-2 having mostly textural details of the source images get fused using a weighted average scheme based on local energy and novel sum modified spatial frequency to preserve the local textures in the fused image. The base layer at scale-2 has only the local luminescence, hence a choose max rule is applied to fuse the base layer to retain better contrast. Moreover, the free parameters of HLD model and

BISFNN are optimized using GWO by considering a fitness function based on spatial frequency [9] and edge index [39] of the fused images to maximize the visual clarity and preservation of structural details, respectively. The salient contributions of the proposed work are outlined as follows:

- This paper presents an optimized CT–MR-T2 neurological image fusion framework using an optimized HLD and BISFNN model that captures the structural and textural details and further enhances the visualization of the fused images.
- Three different fusion rules are designed to fuse each decomposition layer (detail and base layers at a different scale) following the nature of the information carried by the decomposed coefficients to preserve structural, textural, and background information of the source images effectively.
- Instead of successive trails to select the hyper-parameters of conventional ℓ_1 – ℓ_0 HLD and BISFNN model, the GWO approach is applied to compute the optimal values of all parameters.
- In the proposed method, the optimization process is guided by a fitness function based on spatial frequency and edge index of the fused image which maximizes the clarity and preservation of sharp edges present in the source images.

Subsequent sections of this paper are organized as follows: section 2 gives a brief introduction of the methodologies utilized to implement the proposed approach. Section 3 provides the detailed implementation steps involved in the proposed fusion approach. Experimental results and their discussions are presented in section 4. Finally, conclusions are given in section 5.

2. Methodology

2.1. Hybrid $\ell_1 - \ell_0$ Layer Decomposition Model

The hybrid $\ell_1 - \ell_0$ layer decomposition model involves the composite use of ℓ_1 and ℓ_0 regularization factors on base and detail layer, respectively [17]. The piece-wise constant property of ℓ_0 sparsity term helps in better preservation of structural details. On the other hand, ℓ_1 sparsity term holds piece-wise smoothness property which helps in preserving edges, effectively. The mathematical formulation of the hybrid layer decomposition framework is discussed below.

At first level decomposition, $\ell_1 - \ell_0$ priors are imposed on the input image to get first scale components as follows:

$$B_1 = \text{model}_{\ell_1, \ell_0}(I) \quad (1)$$

$$D_1 = I - B_1 \quad (2)$$

where, the input image is denoted by I , B_1 and D_1 represent the base layer and detail layer, respectively at scale 1. The mathematical equation of the decomposition model $\ell_1 - \ell_0$ is given by:

$$\min_B \sum_{p=1}^K \left\{ (I_p - B_p)^2 + \lambda_1 \sum_{i=\{x,y\}} |\partial_i B_p| + \lambda_2 \sum_{i=\{x,y\}} H(\partial_i(I_p - B_p)) \right\} \quad (3)$$

where K and p denote the total number of pixels and the pixel position in the I , B and D . ∂_i represents partial derivative operator along x and y directions. λ_1 and λ_2 are two regularization parameters that control the degree of smoothness of the base layer and detail layer, respectively. The first term is a squared error minimization term which forces the base layer to be close to the input image to preserve most of the information present in the source image. The second term is used to model edge-preserving prior by imposing ℓ_1 gradient sparsity on the base layer. The third term indicates ℓ_0 gradient sparsity imposed on the detail layer as a structural prior using a function $H(x)$:

$$H(x) = \begin{cases} 1, & x \neq 0 \\ 0, & x = 1. \end{cases} \quad (4)$$

The outlier-rejection nature of ℓ_1 sparsity term preserves the important edges present in the base layer. On the other hand, the flattening nature of ℓ_0 sparsity terms effectively preserve structures present in the detail layer. For the second level decomposition, a simplified version of the model given in Eq.(3) is applied to B_1 to capture the texture information as follows:

$$B_2 = \min_B \sum_{p=1}^K \left\{ (B_{1,p} - B_p)^2 + \lambda_3 \sum_{i=\{x,y\}} |\partial_i B_p| \right\} \quad (5)$$

$$D_2 = B_1 - B_2 \quad (6)$$

where B_2 and D_2 represent the base layer and detail layer at scale 2, respectively. The parameter λ_3 controls the degree of smoothness in the base layer B_2 . ℓ_1 gradient sparsity is imposed on base layers to model edge-preserving

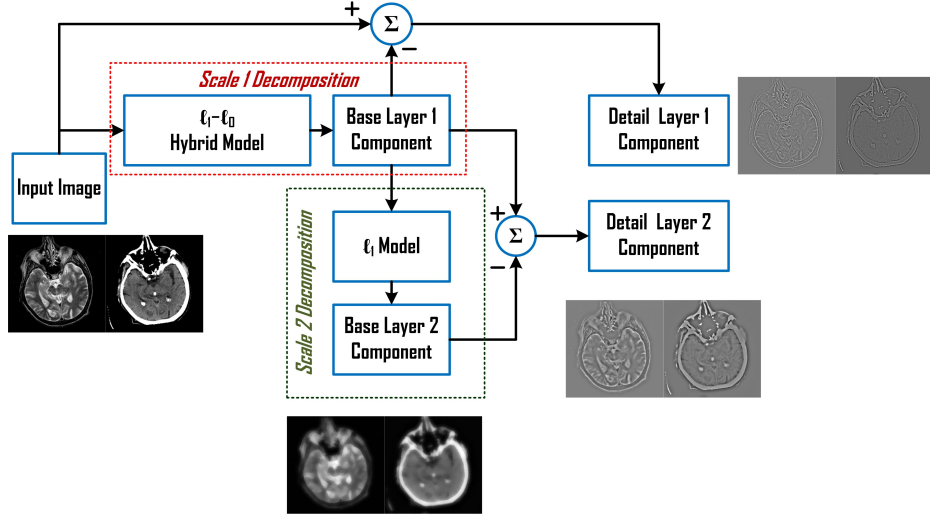


Figure 1: Two scale hybrid $\ell_1-\ell_0$ decomposition model

prior and hence D_2 holds most of the textural information, while B_2 contains only the local mean brightness. A fast joint bilateral filtering of B_2 is also performed using B_1 as a guiding image to regain the sharp edges from its sampled version. Fig. 1 depicts block diagram of two-scale hybrid $\ell_1 - \ell_0$ layer decomposition model. The decomposition model outputs D_1 , D_2 and B_2 containing structural, textural and local mean brightness information of the input image respectively. The original image is reconstructed as by simply adding the decomposed layers follows:

$$I = D_1 + D_2 + B_2 \quad (7)$$

2.2. Biologically Inspired Spiking Feed-forward Neural Model

Bio-Inspired Spiking Feedforward neural network (BISFNN) is a biomimetic design inspired by the visual cortex model of a Human Visual System (HVS) that excites connected neurons based on external input and its characteristics [26]. The feature extraction and feature linking phenomenon of the neuron assemblies present in the visual cortex is captured by a simple neural network model named Pulse Coupled Neural Network (PCNN) [40]. This neural model is a two-dimensional, single-layer network of laterally connected neurons that extract visual features of an image by processing local features and further linking them with the features extracted by the neighbour neurons that help to extract features consistent with human visual perception. Moreover, the internal activities of the neurons are translation,

rotation, illumination, and scale-invariant which makes it more suitable for feature extraction in image processing applications as compared to other methods. Thus, it responds sharply to significant features. The mathematical representation of a simplified version of the BISFNN model is expressed as follows,

$$E_{i,j}(n) = P_{i,j} \quad (8)$$

$$L_{i,j}(n) = e^{-\alpha_L} L_{i,j}(n-1) + V_L \sum_w W_{i,j} Y_{i,j}(n-1) \quad (9)$$

$$U_{i,j}(n) = E_{i,j}(n)(1 + \beta L_{i,j}(n)) \quad (10)$$

$$T_{i,j}(n) = e^{-\alpha_T} T_{i,j}(n-1) + V_T Y_{i,j}(n) \quad (11)$$

$$Y_{i,j}(n) = \begin{cases} 1, & U_{i,j}(n) > T_{i,j}(n) \\ 0, & \text{otherwise} \end{cases} \quad (12)$$

where $P_{i,j}$ is the corresponding pixel intensity or pixel activity at (i, j) which acts as external stimuli to the PCNN neurons. $E_{i,j}$ and $L_{i,j}$ are feeding and linking inputs, respectively. $W_{i,j}$ represents synaptic weights of neighboring neurons within a specified window (w). For a neuron, $U_{i,j}$, $Y_{i,j}$ and $T_{i,j}$ provide their total internal activity, external activity and variable threshold, respectively. n denotes the number of iterations. The conventional BISFNN model has several hyper-parameters such as decay time constant (α_L , α_T), linking parameter (β), internal linking voltage (V_L) and output threshold voltage (V_T) which are selected manually using *hit and trail* approach based on the successive experiments at a regular interval, this may not lead to optimal fusion performance. α_T affects the firing time of the neurons and β controls the extent of modulation of feeding input by linking input. Moreover, they are largely dependent on the nature and texture of the input image. hence it is required to optimize all these free parameters of BISFNN model to get better fusion performance.

2.3. Gray Wolf Optimization

Grey wolf optimization is inspired by the hunting behaviour of grey wolves. It mimics the three phases of social behaviour of a grey wolf pack while hunting their prey namely, tracking, encircling and attacking [19]. There is a four-level of social hierarchy in a pack which are categorized into alpha (α), beta (β), delta (δ) and omega (ω) in descending order of their dominance. The alpha wolves are the leaders and they control the hunting process. The beta wolves execute decisions taken by alpha wolves and lead the pack in their absence. The delta and omega wolves are responsible

for the unity and safety of the pack. The mathematical representation of encircling a prey is depicted by the following formulations:

$$\vec{D} = \left| \vec{C} \cdot \vec{X}_{pr}(k) - \vec{X}_p(k) \right| \quad (13)$$

$$\vec{X}_p(k+1) = \vec{X}_p(k) - \vec{A} \cdot \vec{D} \quad (14)$$

Initially, the wolves are positioned randomly around the prey. Here, $p = 1, 2, \dots, P$ refers to the p^{th} wolf in a group of P grey wolves, \vec{X}_{pr} and \vec{X}_p denote the position vector of prey and the grey wolf respectively, $k = 1, 2, \dots, K$ represent the number of iterations, \vec{A} and \vec{C} denote coefficient vector given as follows:

$$\vec{A} = 2\vec{a} \cdot \vec{r}_1 - \vec{a} \quad (15)$$

$$\vec{C} = 2 \cdot \vec{r}_2 \quad (16)$$

where \vec{a} is a variable that is set to 2 at the beginning and decreased linearly up-to 0 at the end of the maximum iteration. \vec{r}_1 and \vec{r}_2 denote random vectors on the basis of which grey wolves update their position in search space. The mathematical representation of the social hunting nature of grey wolves is expressed by the following equations:

$$\vec{D}_\alpha = \left| \vec{C}_1 \cdot \vec{X}_\alpha - \vec{X}_p \right|, \vec{D}_\beta = \left| \vec{C}_2 \cdot \vec{X}_\beta - \vec{X}_p \right|, \vec{D}_\delta = \left| \vec{C}_3 \cdot \vec{X}_\delta - \vec{X}_p \right| \quad (17)$$

$$\vec{X}_1 = \vec{X}_\alpha - \vec{A}_1 \cdot \vec{D}_\alpha, \vec{X}_2 = \vec{X}_\beta - \vec{A}_2 \cdot \vec{D}_\beta, \vec{X}_3 = \vec{X}_\delta - \vec{A}_3 \cdot \vec{D}_\delta \quad (18)$$

$$\vec{X}_p(k+1) = \frac{\vec{X}_1 + \vec{X}_2 + \vec{X}_3}{3} \quad (19)$$

Alpha (α), beta (β) and delta (δ) wolves participate in hunting as depicted by Eq. 17. Next, the fitness for each of the hunting wolf is evaluated depending on its distance from the prey. The top three fittest wolves are identified and their position is updated using Eq. 18. Next, their positions are saved and averaged together to update the positions of wolves in the next iteration i.e. $\vec{X}_p(k+1)$. In the proposed optimized fusion approach, the optimizer searches for optimal values of eight free parameters ($\lambda_1, \lambda_2, \lambda_3$ for $\ell_1-\ell_0$ HLD model and $\alpha_L, \alpha_T, \beta, V_L, V_T$ for optimized BISFNN model), making the search space eight dimensional i.e. ($N_D = 8$). All the vectors in above mentioned formulations are 1×8 dimensional and each wolf position \vec{X}_p represents a set values of $\lambda_1, \lambda_2, \lambda_3, \alpha_L, \alpha_T, \beta, V_L$ and V_T that is a potential solution to the optimization problem.

3. Proposed Method

This section details the complete implementation steps involved in the process flow of the proposed optimized framework for CT-MR image fusion method which utilizes two scales ℓ_1 – ℓ_0 hybrid decomposition, BISFNN model having optimized parameters using GWO approach. The proposed CT-MR image fusion model based on the aforementioned approach is illustrated in Fig.2.

Step 1: Start with the source CT and MR neurological images referred as $\mathbf{R} = R_{i,j}$ and $\mathbf{S} = S_{i,j}$, respectively, where i and j represent row and column indices.

Step 2: Initialize the GWO parameters i.e. number of search agents (P), number of search variable (N_D), number of maximum iterations (K), position vector (\vec{X}_p), top three fittest wolves (\vec{X}_α , \vec{X}_β , \vec{X}_δ) and variables (\vec{a} , \vec{A} , \vec{C}).

Step 3: Apply two scale hybrid layer ℓ_1 – ℓ_0 decomposition to the source images which provides two details layers and one base layer component.

$$\left[D_{1i,j}^X, D_{2i,j}^X, B_{2i,j}^X \right] = HLD(R_{i,j}) \quad (20)$$

where $D_{1i,j}$ and $D_{2i,j}$ refer to detail layers at scale-1 and scale-2, respectively. $B_{2i,j}$ refers to the base layer components and $X \in (\mathbf{R}, \mathbf{S})$

Step 4: Scale-1 Detail layer fusion – To fuse D_1^X layer components, motivate the BISFNN model by applying the feeding input as scale-1 detail layer coefficients ($D_{1i,j}^X$). Obtain the pulse firing map of neurons ($Y_{i,j}^X$) by the given mathematical relations:

$$E_{i,j}^X(n) = D_{1i,j}^X \quad (21)$$

$$L_{i,j}^X(n) = e^{-\alpha L} L_{i,j}^X(n-1) + V_L \sum_w W_{i,j}^X Y_{i,j}^X(n-1) \quad (22)$$

$$U_{i,j}^X(n) = E_{i,j}^X(n)(1 + \beta L_{i,j}^X(n)) \quad (23)$$

$$T_{i,j}^X(n) = e^{-\alpha T} T_{i,j}^X(n-1) + V_T Y_{i,j}^X(n) \quad (24)$$

$$Y_{i,j}^X(n) = \begin{cases} 1, & U_{i,j}^X(n) > T_{i,j}^X(n) \\ 0, & \text{otherwise,} \end{cases} \quad (25)$$

Step 5: Compute the firing times $ft_{i,j}^X$ in n iteration for which $Y_{i,j}^X = 1$ as follows:

$$ft_{i,j}^X(n) = ft_{i,j}^X(n-1) + Y_{i,j}^X(n) \quad (26)$$

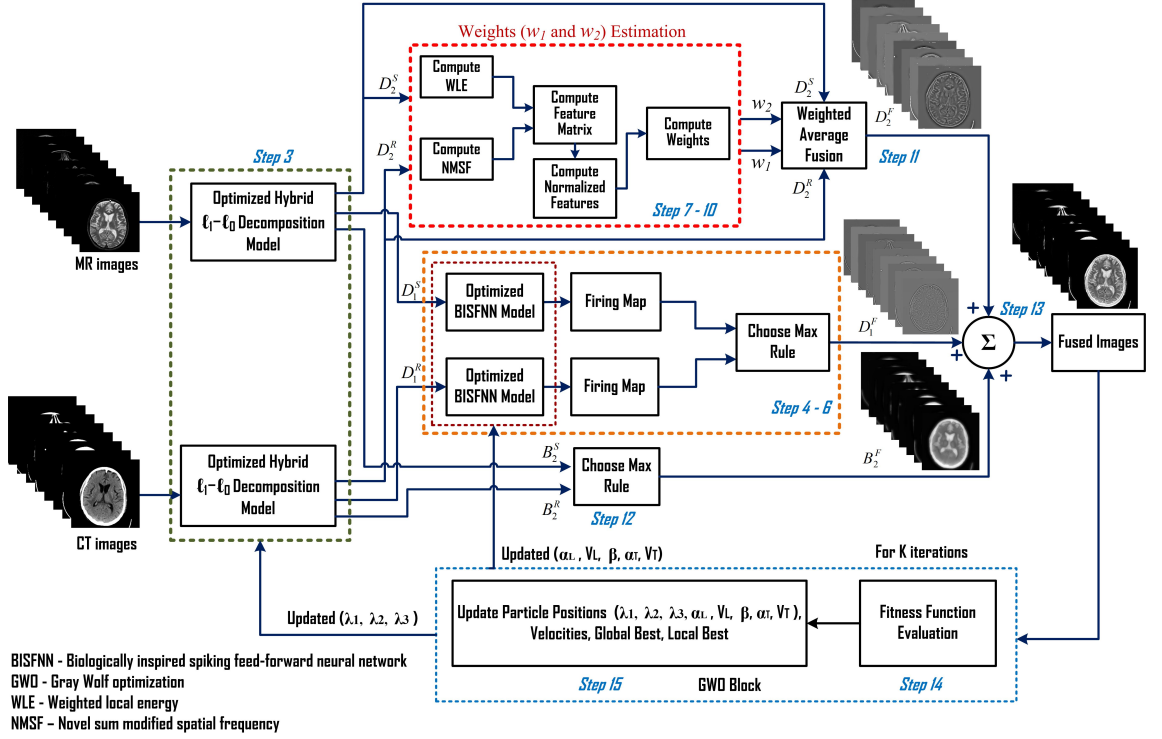


Figure 2: Process flow of the proposed fusion method

Step 6: After maximum iterations $n = n_{max}$, fuse the D_1 layer coefficients based on the firing times evaluated in the previous step as follows:

$$D_{1,i,j}^F = \begin{cases} D_{1,i,j}^R; & ft_{i,j}^R(n) > ft_{i,j}^S(n) \\ D_{1,i,j}^S; & otherwise \end{cases} \quad (27)$$

where $D_{1,i,j}^F$ refers to fused scale-1 detail layer coefficients.

Step 7: Scale-2 Detail layer fusion – To fuse scale-2 detail layer D_2^X components, the concept of weighted averaging is utilized based on the estimation of weighted local energy (WLE) and a novel sum modified spatial frequency ($NMSF$) of $D_{2,i,j}^X$ to preserve the local textures present in source CT and MR images. Estimate weighted local energy and a novel sum modified spatial frequency from scale-2 detail layer (D_2^X) coefficients.

$$WLE_{i,j}^X = \sum_{i=1}^x \sum_{j=1}^y (D_2^X(x+i, y+j)^2 w(i, j)) \quad (28)$$

where $w = \frac{1}{16} \begin{bmatrix} 1 & 4 & 1 \\ 4 & 1 & 4 \\ 1 & 4 & 1 \end{bmatrix}$ denotes $x \times y$ template used for normalization. $x \times y$ denotes the size of the template.

$$NMSF_{i,j}^X = \sqrt{(RF_{i,j}^X)^2 + (CF_{i,j}^X)^2 + \delta} \quad (29)$$

$$RF_{i,j}^X = \sqrt{\frac{1}{M(N-1)} \sum_{i=1}^M \sum_{j=2}^N (D_2^X(i, j-1) - D_2^X(i, j))^2} \quad (30)$$

$$CF_{i,i}^X = \sqrt{\frac{1}{N(M-1)} \sum_{i=2}^M \sum_{j=1}^N (D_2^X(i, j) - D_2^X(i-1, j))^2} \quad (31)$$

$$\delta = \left[\frac{\frac{1}{(M-1)(N-1)} \sum_{i=2}^M \sum_{j=2}^N (D_2^X(i, j) - D_2^X(i-1, j-1))^2 + \frac{1}{(M-1)(N-1)} \sum_{i=2}^M \sum_{j=2}^N (D_2^X(i-1, j) - D_2^X(i, j-1))^2 \right] \quad (32)$$

where $RF_{i,j}^X$ and $CF_{i,i}^X$ refer to the row and column frequency of D_2^X layer, respectively. The third term δ refers to the diagonal frequency of neighborhood pixels.

Step 8: Compute the feature matrix ($FM_{i,j}^X$) as follows:

$$FM_{i,j}^X = WLE_{i,j}^X \cdot NMSF_{i,j}^X. \quad (33)$$

Step 9: Normalize the $FM_{i,j}^X$ in the range [0,1] to get normalized feature matrix $Z_{i,j}^X$ as follows:

$$Z_{i,j}^X = \frac{FM_{i,j}^X - (FM_{i,j}^X)_{min}}{(FM_{i,j}^X)_{max} - (FM_{i,j}^X)_{min}} \quad (34)$$

Step 10: Calculate the weights w_1 and w_2 for D_2^R and D_2^S , respectively as follows:

$$w_1 = \frac{Z_{i,j}^R}{Z_{i,j}^R + Z_{i,j}^S} \quad (35)$$

$$w_2 = \frac{Z_{i,j}^S}{Z_{i,j}^R + Z_{i,j}^S} \quad (36)$$

Step 11: Get the fused layer at scale two D_2^F using weighted average rule as follows:

$$D_{2,i,j}^F = w_1 D_{2,i,j}^R + w_2 D_{2,i,j}^S \quad (37)$$

Step 12: Base layer fusion– Chose max rule is applied to fuse base layer (B_2^X) coefficients and retain better contrast and background information as much as possible.

$$B_{2i,j}^{\mathbf{F}} = \begin{cases} B_{2i,j}^{\mathbf{R}}, & B_{2i,j}^{\mathbf{R}} > B_{2i,j}^{\mathbf{S}} \\ B_{2i,j}^{\mathbf{S}}, & otherwise \end{cases} \quad (38)$$

Step 13: Reconstruct the fused image $\mathbf{F} = F_{i,j}$ as follows:

$$F_{i,j} = D_{1i,j}^{\mathbf{F}} + D_{2i,j}^{\mathbf{F}} + B_{2i,j}^{\mathbf{F}} \quad (39)$$

Step 14: State the fitness function (F_{fit}) as a product of spatial frequency (SF) and edge index ($Q_{RS/F}$) of the fused images as follows:

$$F_{fit} = SF \times Q_{\mathbf{RS}/\mathbf{F}} \quad (40)$$

$$SF = \sqrt{RF^2 + CF^2}, \quad (41)$$

where RF and CF refer to the row and column frequency, respectively and given as,

$$RF = \sqrt{\frac{1}{M(N-1)} \sum_{i=1}^M \sum_{j=2}^N (F(i, j-1) - F(i, j))^2} \quad (42)$$

$$CF = \sqrt{\frac{1}{N(M-1)} \sum_{i=2}^M \sum_{j=1}^N (F(i, j) - F(i-1, j))^2} \quad (43)$$

and

$$Q_{RS/F} = \frac{\sum_{i=1}^M \sum_{j=1}^N \left[Q_{RF}(i, j) w_R(i, j) + Q_{SF}(i, j) w_S(i, j) \right]}{\sum_{i=1}^M \sum_{j=1}^N w_R(i, j) + w_S(i, j)} \quad (44)$$

where Q_{RF} and Q_{SF} denote the edge information preservation [39] values of source CT and MR images weighted by w_R and w_S , respectively.

Step 15: Now, update all aforementioned free parameters using GWO approach by repeating the following steps K times;

1. Evaluate the cost function as defined in step 14.
2. Update the wolf positions using Eqs. 17 - 19.
3. Update the coefficient vectors using Eqs. 15 and 16

Algorithm 1: Proposed Method

Input: Pre-registered CT and MR image pair $R_{i,j}$ and $S_{i,j}$ of size $M \times N$.

Output: Fused image

Parameters: Maximum BISFNN iterations (n_{max}), synaptic weight matrix (W), number of search agents (P), number of search variable (N_D), maximum number of iterations (K), initial particle position (\vec{X}_p)

1. Decompose each source CT and MR image into D_1^X , D_2^X , B_2^X , using Eqs. (1)-(6), where $X \in [R_{i,j}, S_{i,j}]$
 2. **Scale-1 detail layer fusion**
 - Activate the BISFNN model with D_1^X and obtain the pulse firing map of neurons $Y_{i,j}^X$ using Eqs. (21)-(25).
 - Compute the firing times $ft_{i,j}^X$ for n_{max} iteration using Eq. (26).
 - Get the fused detail layer D_1^F at scale-1 using Eq. (27),
 3. **Scale-2 detail layer fusion**
 - Estimate weighted local energy $WLE_{i,j}^X$ and novel sum modified spatial frequency $NMSF_{i,j}^X$ of D_2^X using Eqs. (28)-(32).
 - Compute feature matrix $FM_{i,j}^X$; $FM_{i,j}^X = WLE_{i,j}^X \cdot NMSF_{i,j}^X$, for $X \in [R_{i,j}, S_{i,j}]$
 - Compute normalized feature matrix $Z_{i,j}^X$ using Eq. (34).
 - Calculate the weights w_1 and w_2 for D_2^R and D_2^S , respectively Eqs. (35) and (36)
 - Get the fused detail layer D_2^F at scale-2 using, $D_{2,i,j}^F = w_1 D_{2,i,j}^R + w_2 D_{2,i,j}^S$
 4. **Base layer fusion:** Get the fused base layer B_2^F using choose max rule as Eq. (38).
 5. Get the resultant fused image $F_{i,j}$ by combining fused scale-1 detail layer D_1^F , scale-2 detail layer D_2^F and base layer B_2^F .
 $F_{i,j} = D_{1,i,j}^F + D_{2,i,j}^F + B_{2,i,j}^F$.
 6. State the fitness F_{fit} of the fused image using Eqs. 40-44.
 7. Get updated values of free parameters using GWO by repeating the following steps K times.
 - Evaluate the fitness $F_{fit} = SF \times Q_{RS/F}$ of the fused image.
 - Update the grey wolf positions using Eqs. 17 - 19.
 - Update the coefficient vectors \vec{A} and \vec{C} using Eqs. 15 and 16.
 - Find the top three fittest wolves and update \vec{X}_α , \vec{X}_β , \vec{X}_δ
 - Execute step 1-5 by using updated values of free parameters.
-

4.1. Dataset

To validate the proposed fusion method, several experiments are performed on different CT and MR-T2 neurological image datasets of different

patients taken from the whole brain atlas of the Harvard medical school (<http://www.med.harvard.edu/AANLIB/home.html>). All the CT-MR image pairs are pre-registered and have a spatial resolution of 256×256 . These CT and MR-T2 image datasets have been considered for visual and quantitative evaluation of the fusion images and validated by radiologists.

4.2. Objective Evaluation Metrics

Qualitative results of fusion methods present the comparison of visual assessment among source CT, MR-T2 and fused images, while quantitative evaluation validates the subjective analysis in terms of different performance evaluation parameters. Eleven quantitative parameters such as entropy (EN), standard deviation (SD), mutual information (MI) [41], spatial frequency (SF) [9], edge index ($Q_{RS/F}$) [39], nonlinear correlation information entropy (Q_{NICE}) [42], Peilla Metric (Q) [43], Cvejic Metric (Q_C) [44], Yang Metric (Q_Y) [45], Chen-Blum Metric (Q_{CB}) [46] and $R_Q^{F/RS}$ (with arctangent sigmoid function) [47] are used to evaluate the performance of the proposed CT-MR image fusion method and compare its performance with other state-of-the-art methods. Their mathematical formulations and significance are tabulated in Table 1.

4.3. Implementation and Parameter Settings

In the proposed approach, both the source images are subjected to 2 scale hybrid ℓ_1 - ℓ_0 decomposition into scale-1 and 2 detail layers and one base layer components. To optimize the hyper-parameters of HLD and BISFNN model, GWO technique having $P = 50$ search agents, $K = 12$ iterations and $N_D = 8$ dimensional search space having search variables ($\lambda_1, \lambda_2, \lambda_3, \alpha_L, V_L, \beta, \alpha_T, V_T$) is used. To implement the proposed fusion method, the main challenge is to choose a suitable approach among search techniques available in literature such as Particle Swarm Optimization (PSO) and Differential Evolution Optimization (DEO), Cuckoo Search (CS), etc. [32, 48, 49, 19]. The proposed fusion approach is implemented and tested with other optimization techniques alongwith GWO. The following are the reasons to consider GWO approach in the proposed fusion method.

- For each search algorithm, apart from the number of search agents and iteration number, other control-parameters are also important which need to be initialized and have a great influence on the performance of the search algorithm. For example, PSO requires three control parameters namely inertia coefficient (w), acceleration constants c_1 and c_2 which control the global and local search abilities of the algorithm

Table 1: Quantitative evaluation metrics to analyze the performance of different fusion methods

Sl.No.	Performance Metrics	Mathematical Formulations	Interpretation
1.	Entropy (EN)	$EN = -\sum_{i=0}^{L-1} p(i) \log_2 p(i)$	Higher entropy values refer to more amount of information available in the fused image.
2.	Standard deviation (SD)	$SD = \sqrt{\sum_{i=1}^M \sum_{j=1}^N \frac{F(i,j)-F(i,j)}{M \times N}}$	Higher SD values refer to the fused image with better contrast compared to the source images.
3.	Spatial Frequency (SF) [9]	$SF = \sqrt{RF^2 + CF^2}$, where $RF = \sqrt{\frac{1}{M(N-1)} \sum_{i=1}^M \sum_{j=2}^N (F(i, j-1) - F(i, j))^2}$ $CF = \sqrt{\frac{1}{N(M-1)} \sum_{i=2}^M \sum_{j=1}^N (F(i, j) - F(i-1, j))^2}$	Higher SF values refer to better visual clarity.
4.	Mutual Information (MI) [41]	$MI = I(x_R; x_F) + I(x_S; x_F)$	Higher MI values depict more visual information transferred from input to fused images
5.	Edge index ($Q_{RS/F}$) [39]	$Q_{RS/F} = \frac{\sum_{i=1}^M \sum_{j=1}^N Q_{RF(i,j)} w_R(i,j) + Q_{SF(i,j)} w_S(i,j)}{\sum_{i=1}^M \sum_{j=1}^N w_R(i,j) + w_S(i,j)}$	Higher $Q_{RS/F}$ values indicate better preservation of edge information in fused images.
6.	Nonlinear Correlation Information Entropy (Q_{NICE}) [42]	$Q_{NICE} = 1 + \sum_{i=1}^k \frac{\lambda_i^{R^N}}{k} \log_k \frac{\lambda_i^{R^N}}{k}$	Higher Q_{NICE} values indicate more correlation between the source and fused images.
7.	Peilla Metric (Q) [43]	$Q = \frac{1}{W} \sum_{w \in W} [\lambda_R(w) Q_0(R, F w) + \lambda_S(w) Q_0(S, F w)]$	Higher values of Q gives the extent up to which the fused image retains the salient information contained within the source images.
8.	Cvejic Metric (Q_C) [44]	$Q_C = \sum_{w \in W} \left[\frac{sim(R, S, F w) Q(R, F w) + (1 - sim(R, S, F w)) Q(S, F w)}{2} \right]$	Higher Q_C value refers more similarity between fused and reference images.
9.	Yang Metric (Q_Y) [45]	$Q_Y = \frac{1}{ W } \sum_{w \in W} Q(R, S, F w)$	Higher Q_Y values indicate better preservation of complementary information in the fused images.
10.	Chen and Blum Metric (Q_{CB}) [46]	$Q_{CB} = mean(\lambda_R(i, j) Q_{RF}(i, j) + \lambda_S(i, j) Q_{SF}(i, j))$	Higher Q_{CB} values measure the quality of fused images based on human vision system.
11.	Fractional order differentiation based edge information ($R_Q^{F/RS}$) [47]	$R_Q^{F/RS} = \frac{\sum_{i=1}^M \sum_{j=1}^N (R^{FR}(i,j) W^R(i,j) + R^{FS}(i,j) W^S(i,j))}{\sum_{i=1}^M \sum_{j=1}^N W^R(i,j) + W^S(i,j)}$	Higher $R_Q^{F/RS}$ values indicate presence of more edge information in the fused image.

[48]. Similarly, in the case of DEO, parameters like scaling factor (FR) and crossover rate of (CR) need to be selected properly to get optimal performance [49]. The selection of all these control parameters (usually, done by the hit and trial approach) is very crucial to ensure the efficacy of the search algorithm. Also sometimes, this becomes time-consuming and may lead to inaccurate solutions. While GWO can be regarded as a parameter-less algorithm in which all the internal control parameters are updated automatically using two vectors \vec{r}_1 and \vec{r}_2 selected randomly between 0 to 1 which further reduces manual

interventions [19].

- To justify the consideration of the GWO approach, extensive experiments are carried out on several CT and MR-T2 image pairs wherein the source images were subjected to fusion using the proposed method with PSO, DEO and GWO techniques. For each optimization technique, same fitness function, number of search agents (50) and maximum number of iterations (12) are considered. The visual results obtained for all the cases were found approximately similar. Furthermore, all objective measures are computed in each case and their averaged values are tabulated in Table 2 from which it is observed that all three optimization techniques give similar fusion performance and achieve approximately the same optimal solution.
- Moreover, another comparison is made among the optimization time taken by each technique and presented in Table 3. From the results, it is observed that for the same number of search agents and iterations, GWO takes 10% less time as compared to other algorithms which helps in improving the computational efficiency of the proposed fusion approach.

Based on the above discussion, GWO offers optimal performance along with reduced computational complexity and manual intervention as compared to others. Therefore, GWO has been selected for the present study.

Table 2: Averaged performance analysis of different optimization algorithms for CT-MR image fusion

Performance Metrics	Optimization Algorithm		
	PSO	DEO	GWO
EN	4.959 ± 0.285	4.964 ± 0.284	4.943 ± 0.283
SD	83.757 ± 4.666	83.720 ± 4.660	83.960 ± 4.593
SF	7.178 ± 0.619	7.181 ± 0.621	7.186 ± 0.621
MI	3.203 ± 0.235	3.202 ± 0.237	3.224 ± 0.258
$Q_{RS/F}$	0.588 ± 0.043	0.588 ± 0.042	0.588 ± 0.044
Q_{NICE}	0.808 ± 0.001	0.808 ± 0.001	0.808 ± 0.001
Q	0.826 ± 0.028	0.826 ± 0.028	0.826 ± 0.028
Q_C	0.710 ± 0.055	0.710 ± 0.055	0.710 ± 0.055
Q_Y	0.778 ± 0.051	0.778 ± 0.050	0.779 ± 0.054
Q_{CB}	0.633 ± 0.064	0.631 ± 0.064	0.633 ± 0.064
$R_Q^{F/RS}$	0.351 ± 0.007	0.351 ± 0.007	0.351 ± 0.007

After selection of GWO as an optimization technique, another challenge is to decide a suitable termination criterion for the GWO algorithm. Deciding the number of iteration k is a very crucial step to maintain a balance

Table 3: Average run-time analysis of different optimization algorithms for CT-MR image fusion

Optimization Schemes	Average running time (seconds)
PSO	436.07 ± 8.71
DEO	435.39 ± 6.80
GWO	392.44 ± 3.67

between the algorithm’s computational efficiency and optimization performance. For a proper selection of maximum iteration number, extensive experiments were carried out to analyze the effect of iterations on a fitness function. Out of them, some results are presented in Fig. 4 (a)-(f). From Fig. 4, it is observed that the optimizer search converges at the 8th iteration for some cases while in few cases (refer Fig. 4 (d)-(f)), the fitness improves up to the 10th iteration but does not improve further by a notable gain. Similar kinds of observations were made for the rest of the fusion cases. Thus, based on the experimental results, maximum iterations $k = 12$ is considered for the GWO while implementing the proposed fusion method.

For GWO algorithm, the search variables are initialized to (\vec{X}_p) to $(0, 0, 0, 0, 0, 0, 0, 10)$ with an upper bound of $(1, 1, 1, 1, 1, 3, 1, 20)$. \vec{a} is set to 2 and decreases further up-to 0 at the end of the maximum iteration while \vec{r}_1 and \vec{r}_2 denote random vectors and hence selected randomly between 0 to 1 [19]. The maximum iteration $n_{max} = 150$ and $W = [0.707 \ 1 \ 0.707; 1 \ 0 \ 1; 0.707 \ 1 \ 0.707]$ are chosen for BISFNN model.

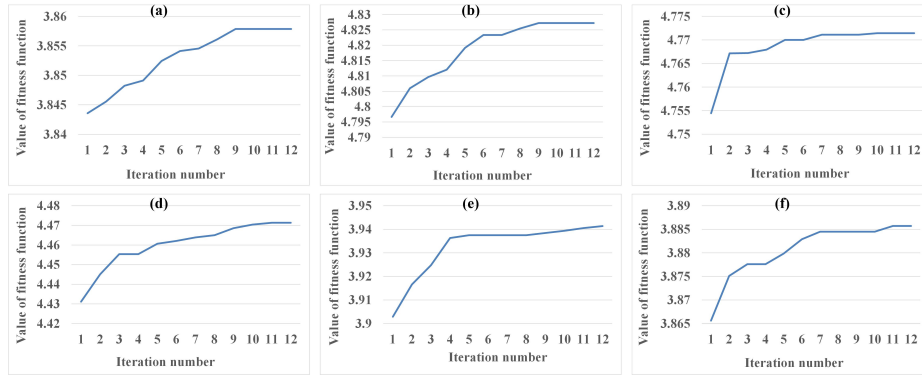


Figure 4: Fitness value vs iteration count of GWO for different CT-MR image pairs.

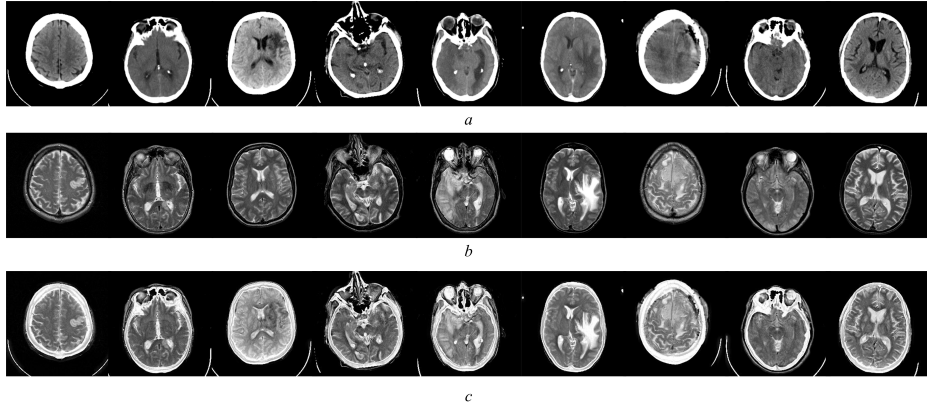


Figure 5: Source (a) CT images, (b) MR images, and (c) Fused images obtained by our proposed fusion method.

4.4. Results and Analysis

4.4.1. Experiment 1

In this experiment, the fusion performance is analyzed for CT and MR-T2 image dataset out of which nine CT-MR image pairs are shown in Fig. 5(a) and Fig. 5(b), respectively. The corresponding fused images obtained by the proposed method are shown in Fig. 5(c). From the results shown in Fig. 5(c), it is observed that the fusion method integrates the complementary information present in the source images. The fused images demarcate the skull boundaries and also preserve the edges and contrast of soft tissues effectively. Moreover, the fused image carries composite information of both the source images that can lead to more factual interpretations and accurate clinical diagnosis. To validate the visual performance, objective evaluation metrics are evaluated and presented in Table 4 from which it is observed that the proposed fusion method yields significant values for all aforementioned quantitative measures. Furthermore, another comparison is shown in Fig. 6 to quantify the fusion results between fused and source CT-MR-T2 images in terms of EN , SD , and SF values illustrated in Figs. 6(a), 6(b) and 6(c), respectively. To give a better insight into the overall performance of the proposed fusion algorithm, averaged values of EN , SD and SF are presented in Table 5. The proposed fusion method gets approx. 61.27% and 27.4% higher EN , 0.06% and 41.46% higher SD , 36.40% and 13.51% higher SF values than the source CT and MR-T2 images, respectively. Higher EN values indicate that the fusion results carry more diagnostic information than an individual source image. Higher SD and SF show that the fused

Table 4: Performance evaluation metrics obtained by the proposed method for the fused images shown in **Fig. 5**

Performance Metrics	Image Pairs								
	#1	#2	#3	#4	#5	#6	#7	#8	#9
EN	5.392	4.929	4.864	5.384	4.96	4.651	4.572	4.901	4.831
SD	81.74	78.44	88.83	79.96	85.78	82.51	93.15	82.26	82.99
SF	6.651	7.457	6.757	8.410	7.691	6.392	6.816	7.175	7.320
MI	3.710	3.328	2.840	3.039	3.132	3.224	3.488	3.067	3.187
$Q_{RS/F}$	0.592	0.624	0.522	0.573	0.581	0.603	0.600	0.664	0.530
Q_{NICE}	0.809	0.807	0.806	0.806	0.807	0.807	0.808	0.806	0.807
Q	0.819	0.857	0.774	0.804	0.823	0.858	0.826	0.856	0.810
Q_C	0.820	0.748	0.611	0.707	0.710	0.699	0.688	0.698	0.703
Q_Y	0.848	0.817	0.668	0.794	0.791	0.758	0.743	0.824	0.760
Q_{CB}	0.500	0.681	0.600	0.585	0.625	0.702	0.681	0.685	0.635
$R_Q^{F/RS}$	0.352	0.357	0.340	0.346	0.354	0.360	0.348	0.360	0.342

image has better contrast and clarity which makes the fused images visually better than both the source CT and MR-T2 images. From the experimental results, it is concluded that the proposed method can improve the visualization of the fused images with better contrast and clarity than the source images.

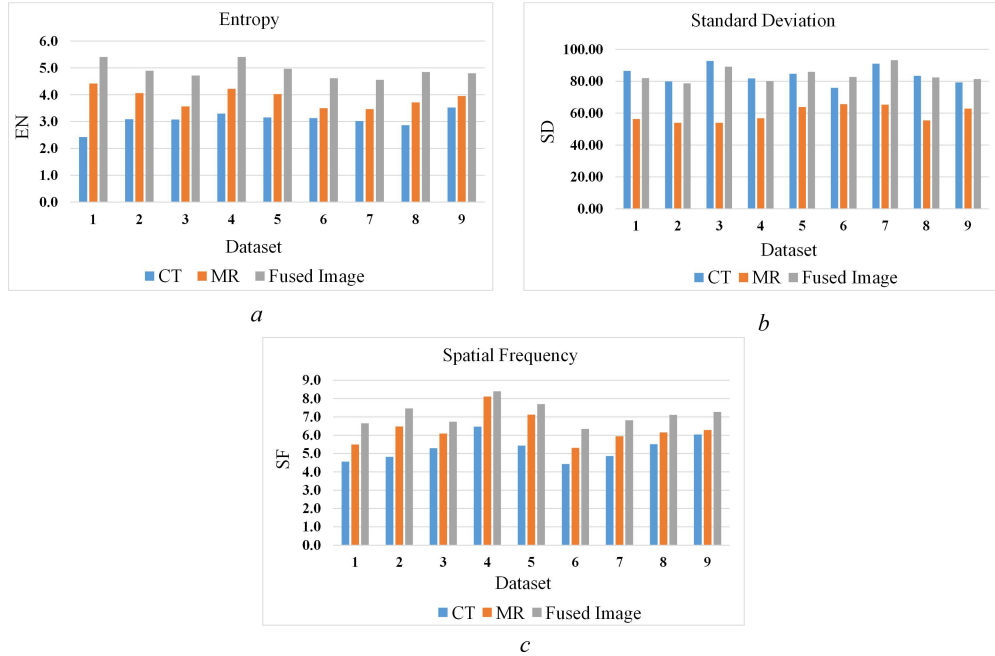


Figure 6: Bar graph illustrating the performance of the proposed method compared with the reference CT and MR for (a) EN (b) SD (c) SF

Table 5: Averaged performance metrics (mean \pm standard deviation) of source CT, MR and the fused images obtained by the proposed method.

Source Images	Performance Metrics		
	EN	SD	SF
CT	3.065 ± 0.304	83.908 ± 5.495	5.268 ± 0.678
MR	3.880 ± 0.337	59.351 ± 4.984	6.331 ± 0.852
Proposed	4.943 ± 0.283	83.960 ± 4.593	7.186 ± 0.621

4.4.2. Experiment 2

In this section, a comparative analysis is done to highlight the efficacy of the proposed fusion method compared to nine other state-of-the-art fusion approaches in the terms of both qualitative and quantitative performance. For comparison, five pairs of source CT and MR-T2 images are shown in Figs. 7–11 (a) and (b), respectively. Moreover, two zoomed regions are presented to visualize a clear demarcation between the performance of the proposed and other existing fusion methods. The results of fusion performance obtained by the proposed fusion method are compared with the following nine state-of-the-art fusion approaches,

Method 1: Convolutional sparse representation (CSR) based fusion method proposed by Liu et al. (2016) and discussed in [35]. Base layers are fused using an averaging scheme. Detail layers are fused by first obtaining their sparse coefficient maps using the CSR model followed by choose max rule.

Method 2: Convolutional neural network (CNN) based medical image fusion method presented by Liu et al. (2017) as discussed in [37] in which weight map and local energy map are calculated after decomposing the source images using Laplacian pyramid.

Method 3: NSST domain adaptive PCNN based fusion model proposed by Yin et al. (2018) as described in [25]. Source images are decomposed using 3-level NSST and the adaptive PCNN is used further to fuse high-frequency subbands. For PCNN $W = [0.5 \ 1 \ 0.5; 1 \ 0 \ 1; 0.5 \ 1 \ 0.5]$ and $n_{max} = 110$

Method 4: Fusion approach proposed by Ramlal et al. (2018) [13] in which images are first subjected to 3-level NSST. Low-frequency subbands are fused using choose max rule based on regional energy followed by consistency verification and high-frequency subbands are fused using PCNN activated by morphological gradients of coefficients. The PCNN has fixed parameters as $W = [0.707 \ 1 \ 0.707; 1 \ 0 \ 1; 0.707 \ 1 \ 0.707]$, $n_{max} = 150$, $\alpha_L = 0.3$,

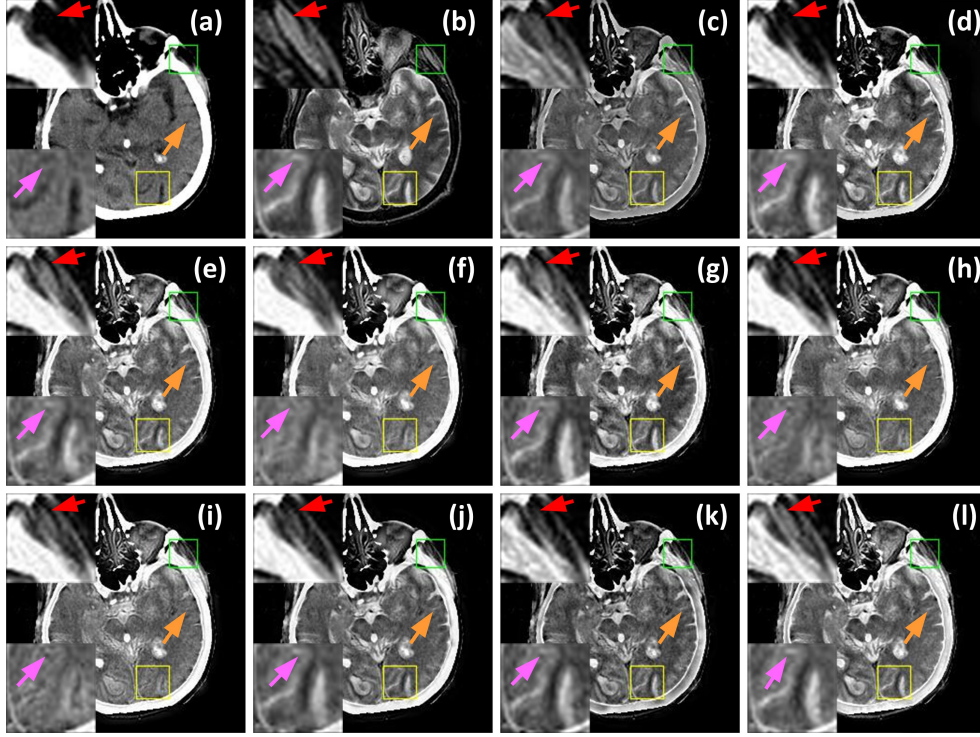


Figure 7: Visual comparison of (a) CT image (b) MR image and fused images obtained by (c) Liu et al. (2016) [35] (d) Liu et al. (2017) [37] (e) Yin et al. (2018) [25] (f) Ramlal et al. (2018)[13] (g) Ganasala et al. (2019) [15] (h) Zhu et al. (2019) [10] (i) Li et al. (2020) [11] (j) Tan et al. (2020) [14] (k) Panigrahy et al. (2020) [31] (l) Proposed method

$\alpha_T = 0.1$, $\beta = 0.2$, $V_L = 1$ and $V_T = 10$.

Method 5: Fusion approach presented by Ganasala et al. (2019) [15] in the SWT domain. Source images are subjected to three-level SWT. Approximate subband coefficients are fused based on texture energy features, while detail subband components get fused using maximum selection rule.

Method 6: NSCT domain fusion method presented by Zhu et al. (2019) [10]. 3-level NSCT decomposition is performed on the source images. Low-frequency subbands are fused taking into account the local Laplacian energy. High-frequency subbands fusion is based on local phase congruency, sharpness, and energy.

Method 7: Fusion approach by Li et al. [11] (2020) in which source images are decomposed using 3-level NSCT. Low-frequency subbands are fused

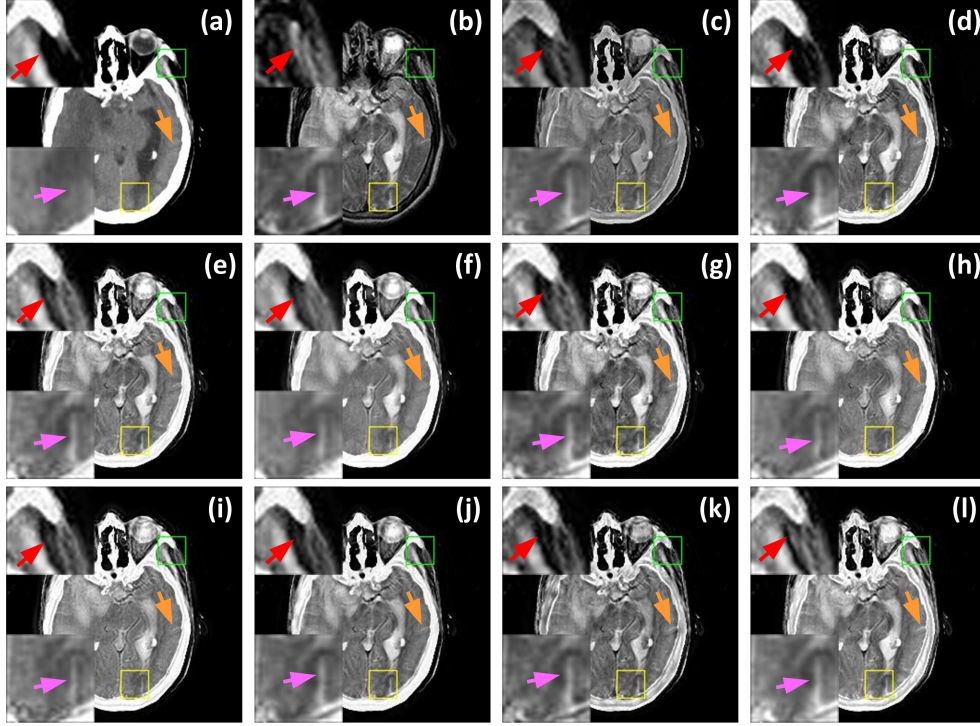


Figure 8: Visual comparison of (a) CT image (b) MR image and fused images obtained by (c) Liu et al. (2016) [35] (d) Liu et al. (2017) [37] (e) Yin et al. (2018) [25] (f) Ramlal et al. (2018)[13] (g) Ganasala et al. (2019) [15] (h) Zhu et al. (2019) [10] (i) Li et al. (2020) [11] (j) Tan et al. (2020) [14] (k) Panigrahy et al. (2020) [31] (l) Proposed method

using regional standard deviation. High-frequency subbands are fused using coefficient activated PCNN. The PCNN uses fixed parameters as $W = [0.707 \ 1 \ 0.707; 1 \ 0 \ 1; 0.707 \ 1 \ 0.707]$, $n_{max} = 150$, $\alpha_L = 0.3$, $\alpha_T = 0.1$, $\beta = 0.2$, $V_L = 1$ and $V_T = 10$.

Method 8: NSST domain fusion approach given by Tan et al. [14] (2020). Low-frequency coefficients are fused with the help of energy attributes and high-frequency coefficients are fused using bounded measure PCNN. The PCNN has fixed parameters as $n_{max} = 200$, $\alpha_L = 0.02$, $\alpha_T = 3$, $\beta = 3$, $V_L = 1$, $V_T = 20$ and the size of W is 7×7 .

Method 9: A parameter adaptive Fusion approach presented by Panigrahy et al. [31] (2020) in the NSST domain. 4-level NSST decomposition is performed on the source images. Low-frequency coefficients are fused using multi-scale morphological gradient and high-frequency coefficients are fused

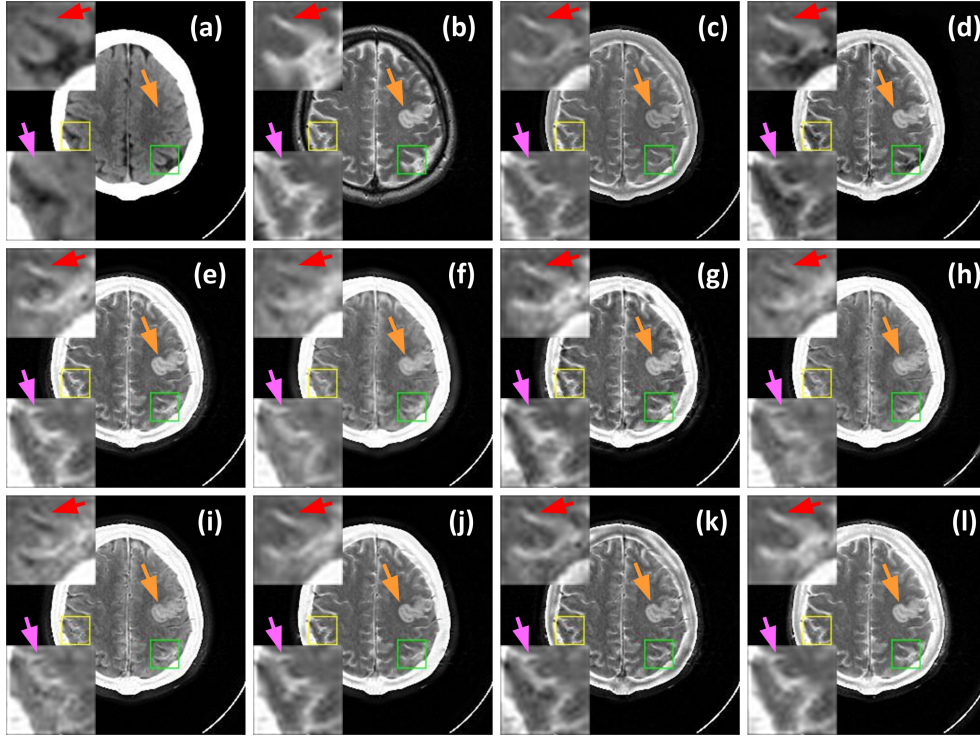


Figure 9: Visual comparison of (a) CT image (b) MR image and fused images obtained by (c) Liu et al. (2016) [35] (d) Liu et al. (2017) [37] (e) Yin et al. (2018) [25] (f) Ramlal et al. (2018)[13] (g) Ganasala et al. (2019) [15] (h) Zhu et al. (2019) [10] (i) Li et al. (2020) [11] (j) Tan et al. (2020) [14] (k) Panigrahy et al. (2020) [31] (l) Proposed method

using parameter adaptive dual-channel PCNN. $W = [0.5 \ 1 \ 0.5; 1 \ 0 \ 1; 0.5 \ 1 \ 0.5]$ and $n_{max} = 150$ is used For PCNN.

A) Qualitative Analysis of CT and MR-T2 Neurological Images

The fused images (Fig. 7-11 (c)) obtained by Liu et al. (2016) [35] method suffer from the limited contrast and so, it fails sometimes to present a significant demarcation of the skull boundary and soft tissue structures. Liu et al. (2017) [37] and Yin et al. (2018) [25] methods offer more preservation of soft tissue edges depicted by Fig. 7-11 (d) and (e), respectively. However, in some regions, the proposed method performs better (refer to the zoomed regions and arrows marked in Figs. 7-11 (d), (e) and (l)). Ramlal et al. (2018) [13], Ganasala et al. (2019) [15] and Zhu et al. (2019) [10] fusion methods also provide better hard tissue and soft tissue contrast which can be visualized from Fig. 7-11 (f), (g) and (h). However, they lack

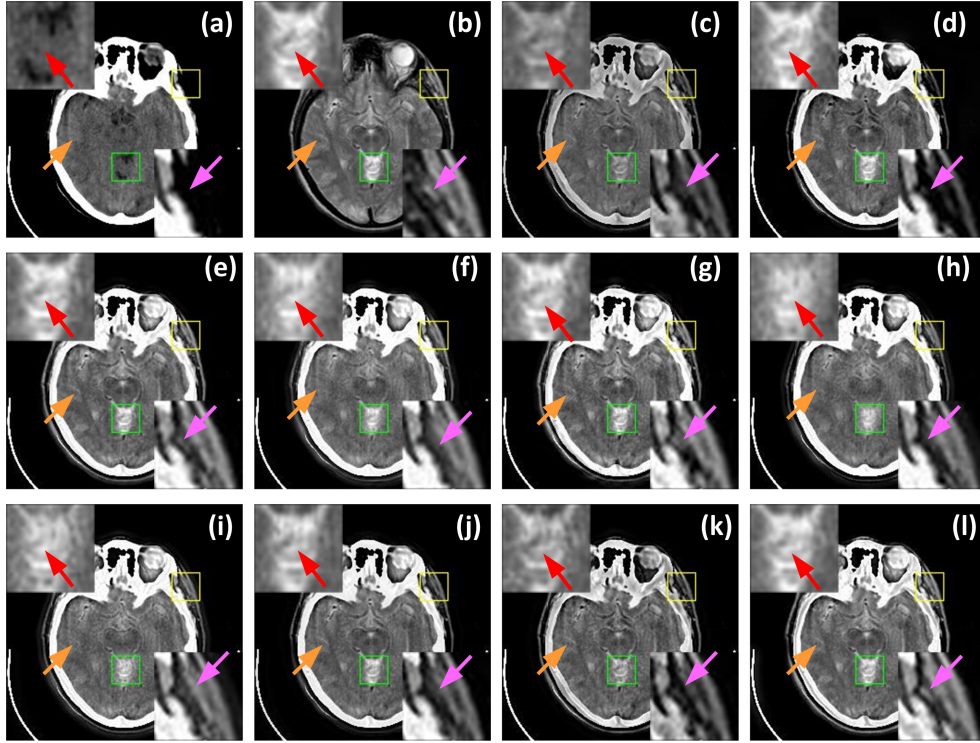


Figure 10: Visual comparison of (a) CT image (b) MR image and fused images obtained by (c) Liu et al. (2016) [35] (d) Liu et al. (2017) [37] (e) Yin et al. (2018) [25] (f) Ramlal et al. (2018)[13] (g) Ganasala et al. (2019) [15] (h) Zhu et al. (2019) [10] (i) Li et al. (2020) [11] (j) Tan et al. (2020) [14] (k) Panigrahy et al. (2020) [31] (l) Proposed method

to preserve the important diagnostic edge details present in source MR-T2 images. Moreover, the results obtained by Ramlal et al. (2018) [13] and Zhu et al. (2019) [10] methods do not provide much clarity of textures as compared to the proposed method that can also be visualized from the zoomed version of the considered regions shown in Figs. 7-11, (f), (h) and (l), respectively. Ganasala et al. (2019) [15] method gives fused images with better contrast and clarity, but the sharp edges present in MR-T2 images are reflected by the proposed method in a better way. From Fig. 7-11 (i) and (j), it can be observed that the Li et al. (2020) [11] and Tan et al. (2020) [14] methods can not reflect edge information and structural details of the soft tissues available in the source MR images properly. Panigrahy et al. (2020) [31] approach preserves the soft tissue structures well (refer Fig. 7-11 (k)) but suffers from limited contrast in some cases and cease to

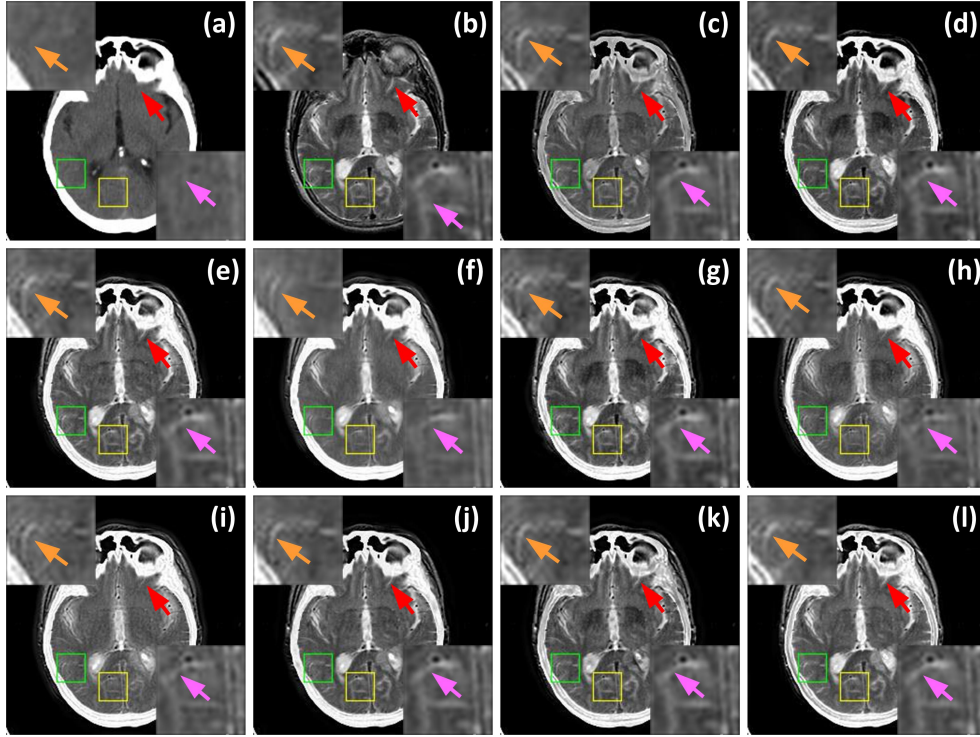


Figure 11: Visual comparison of (a) CT image (b) MR image and fused images obtained by (c) Liu et al. (2016) [35] (d) Liu et al. (2017) [37] (e) Yin et al. (2018) [25] (f) Ramlal et al. (2018)[13] (g) Ganasala et al. (2019) [15] (h) Zhu et al. (2019) [10] (i) Li et al. (2020) [11] (j) Tan et al. (2020) [14] (k) Panigrahy et al. (2020) [31] (l) Proposed method

demarcate the skull boundaries. From the comparative analysis and discussion of the aforementioned fusion performance, it can be inferred that the proposed fusion approach outperforms the existing state-of-the-art fusion methods developed recently and also is able to preserve the sharp edge and the important diagnostic features with better local contrast and texture clarity.

B) Qualitative Analysis – Visual Interpretation by the Radiologist

CT-MR image pair shown in Fig. 7 is a case of multiple infarcts wherein infarct is noted in the right medial temporal lobe which is very well visualized in the MR image due to the excellent soft tissue delineation in MR images. However in the analogous section of CT images, the infarct is not well visualized. In the fused image shown in Fig. 7 (l), the infarct can be clearly detected. Fig. 8 presents a case of fatal stroke where both CT-MR

images show large infarct with edema in the right temporo parietal region with mass effect in the form of shift of midline structure (midbrain) to the left and effacement of the sulcogyral spaces. However, in the fused image shown in Fig. 8 (l) the involved area is well delineated and the adjacent structures are well seen. Fig. 9 shows a case of acute stroke presenting as speech arrest. Here, the cortical involvement of the infarct in the left frontal lobe which is very subtle to be picked up on CT, is very well visualized in the fused image shown in Fig. 9 (l). Fig. 10 presents a case hypertensive encephalopathy where areas of cortical hyperintensities are noted on MR while these findings are not so clearly visualized on CT. The fused image shown in Fig. 10 (l) is able to integrate source anatomical information very well. The CT-MR pair shown in Fig. 11 is a case of acute stroke (writes but cannot read). MR image shows an infarct involving the medial aspect of occipital lobe and left side of splenium of corpus callosum which is very well diagnosed with the help of the fused image shown in Fig. 11 (l).

Table 6: Performance comparison of the proposed method with existing fusion methods for CT-MR pair-1 shown in Fig. 7

Performance Metrics	Fusion Methods									
	Liu et al. [35] (2016)	Liu et al. [37] (2017)	Yin et al. [25] (2018)	Ramial et al. [13] (2018)	Gansala et al. [15] (2019)	Zhu et al. [10] (2019)	Li et al. [11] (2020)	Tan et al. [14] (2020)	Panigrahy et al. [31] (2020)	Proposed Method
<i>EN</i>	4.9006	5.3052	5.3538	5.3596	5.3683	5.1521	5.4769	5.3044	5.3619	5.384
<i>SD</i>	62.5036	80.4816	83.1894	83.8488	82.3326	83.0031	82.7233	79.5201	71.5075	79.9589
<i>SF</i>	7.5499	7.9461	8.2453	7.4394	8.4438	7.6880	8.0928	7.6733	8.4831	8.4105
<i>MI</i>	2.5390	2.6921	2.8574	2.8806	2.7449	2.7546	2.7775	2.7466	2.5922	3.0395
<i>Q_{RSIF}</i>	0.5535	0.5561	0.5402	0.5195	0.5159	0.5126	0.514	0.5311	0.5431	0.5739
<i>Q_{NICE}</i>	0.8053	0.8057	0.8061	0.8062	0.8058	0.8059	0.8059	0.8058	0.8054	0.8066
<i>Q</i>	0.7860	0.7442	0.7933	0.7440	0.7756	0.7542	0.7499	0.7659	0.7849	0.8048
<i>Q_C</i>	0.6125	0.5727	0.6357	0.6623	0.6519	0.6676	0.6501	0.6129	0.6591	0.7077
<i>Q_Y</i>	0.7305	0.7177	0.7774	0.7348	0.7443	0.7446	0.7245	0.7490	0.7443	0.7943
<i>Q_{CB}</i>	0.5823	0.5572	0.5849	0.5390	0.5695	0.5582	0.5207	0.5599	0.5818	0.5850
<i>R_Q^{F/RS}</i>	0.340	0.3350	0.3414	0.3305	0.3367	0.3306	0.3348	0.3317	0.3405	0.3461

Table 7: Performance comparison of the proposed method with existing fusion methods for CT-MR pair-2 shown in Fig. 8

Performance Metrics	Fusion Methods									
	Liu et al. [35] (2016)	Liu et al. [37] (2017)	Yin et al. [25] (2018)	Ramial et al. [13] (2018)	Gansala et al. [15] (2019)	Zhu et al. [10] (2019)	Li et al. [11] (2020)	Tan et al. [14] (2020)	Panigrahy et al. [31] (2020)	Proposed Method
<i>EN</i>	4.5888	4.7646	4.8911	4.9511	4.9458	4.8282	5.0727	4.9341	5.0098	4.9605
<i>SD</i>	66.8347	84.9477	89.1694	89.9994	87.675	88.731	88.5985	85.2121	76.0891	85.7764
<i>SF</i>	6.9852	7.3057	7.4909	6.4065	7.6857	7.1346	7.3393	7.0730	7.7719	7.6916
<i>MI</i>	2.6221	2.7690	2.9749	3.0434	2.8673	2.8893	2.9184	2.9048	2.6786	3.1321
<i>Q_{RSIF}</i>	0.5564	0.5624	0.5308	0.5025	0.5101	0.502	0.5080	0.5231	0.5463	0.5813
<i>Q_{NICE}</i>	0.8058	0.8062	0.8067	0.8069	0.8064	0.8065	0.8065	0.8065	0.8059	0.8072
<i>Q</i>	0.8141	0.8029	0.8085	0.7526	0.7913	0.7828	0.7744	0.7925	0.8018	0.8236
<i>Q_C</i>	0.6423	0.6167	0.6347	0.6369	0.6491	0.6901	0.6241	0.613	0.6543	0.7102
<i>Q_Y</i>	0.7443	0.7505	0.7720	0.7099	0.7437	0.7173	0.7143	0.7566	0.7398	0.7915
<i>Q_{CB}</i>	0.6218	0.6222	0.6258	0.5757	0.5852	0.5908	0.5684	0.6068	0.6088	0.6254
<i>R_Q^{F/RS}</i>	0.3504	0.3476	0.3498	0.3359	0.3437	0.3414	0.3446	0.3407	0.3488	0.3548

C) Quantitative Analysis – Parametric Evaluation

To validate the visual performance, quantitative performance metrics are evaluated for all aforementioned fusion approaches and presented in Tables 6-10 for fused images shown in Figs. 7-11, respectively. The proposed method provides a significant increment in all quantitative measures and

Table 8: Performance comparison of the proposed method with existing fusion methods for CT-MR pair-3 shown in Fig. 9

Performance Metrics	Fusion Methods									Proposed Method
	Liu et al. [35] (2016)	Liu et al. [37] (2017)	Yin et al. [25] (2018)	Ramlal et al. [13] (2018)	Gansala et al. [15] (2019)	Zhu et al. [10] (2019)	Li et al. [11] (2020)	Tan et al. [14] (2020)	Panigrahy et al. [31] (2020)	
<i>EN</i>	4.9485	5.1695	5.3476	5.3322	5.3618	5.3226	<u>5.3751</u>	5.2051	5.3280	5.3922
<i>SD</i>	66.3672	78.2407	85.3476	86.6213	83.042	85.7214	<u>85.7797</u>	83.3019	71.3589	81.7371
<i>SF</i>	6.0501	6.2222	6.4184	5.3791	6.6890	5.8447	6.0481	5.8022	6.8850	6.6516
<i>MI</i>	3.1407	2.8583	<u>3.4355</u>	3.319	3.2378	3.2705	3.3392	3.2757	3.2031	3.7108
<i>Q_{RS/F}</i>	0.5754	0.5391	0.5102	0.4566	0.4948	0.4436	0.4750	0.4980	<u>0.5769</u>	0.5925
<i>Q_{NICE}</i>	0.8072	0.8063	<u>0.8081</u>	0.8076	0.8075	0.8075	0.8077	0.8076	0.8075	0.8094
<i>Q</i>	0.7912	0.6933	0.7986	0.7506	0.7782	0.7566	0.7648	0.7818	0.8271	<u>0.8193</u>
<i>Q_C</i>	0.5692	0.6042	0.7140	0.6902	0.7214	0.7078	0.7082	0.6508	<u>0.7723</u>	0.8308
<i>Q_Y</i>	0.5938	0.6802	0.7887	0.7187	0.7342	0.7398	0.7417	0.7292	<u>0.7923</u>	0.8486
<i>Q_{C-B}</i>	<u>0.5202</u>	0.4876	0.5019	0.4492	0.5063	0.4266	0.4328	0.5035	0.5252	0.5005
<i>R_Q^{F/RS}</i>	<u>0.3459</u>	0.3214	0.3334	0.3171	0.3316	0.3178	0.3255	0.3289	0.3452	0.3524

Table 9: Performance comparison of the proposed method with existing fusion methods for CT-MR pair-4 shown in Fig. 10

Performance Metrics	Fusion Methods									Proposed Method
	Liu et al. [35] (2016)	Liu et al. [37] (2017)	Yin et al. [25] (2018)	Ramlal et al. [13] (2018)	Gansala et al. [15] (2019)	Zhu et al. [10] (2019)	Li et al. [11] (2020)	Tan et al. [14] (2020)	Panigrahy et al. [31] (2020)	
<i>EN</i>	4.3929	5.1791	4.7765	4.8870	4.7964	4.7235	<u>5.1546</u>	4.9262	4.8533	4.9015
<i>SD</i>	65.0448	81.9095	84.2222	84.8278	83.9126	<u>84.2902</u>	83.9789	80.4735	74.1379	82.2559
<i>SF</i>	6.4130	6.7178	6.9094	6.4242	7.1225	6.4980	6.8482	6.4027	<u>7.1553</u>	7.1759
<i>MI</i>	2.7149	2.7873	<u>2.9351</u>	2.8880	2.8057	2.8596	2.8344	2.8423	2.7425	3.0672
<i>Q_{RS/F}</i>	0.6126	0.6348	0.6239	0.5870	0.6072	0.5888	0.5983	0.5908	<u>0.6371</u>	0.6649
<i>Q_{NICE}</i>	0.8058	0.8061	<u>0.8064</u>	0.8063	0.8061	0.8063	0.8062	0.8062	0.8059	0.8068
<i>Q</i>	0.8460	0.7687	<u>0.8531</u>	0.7998	0.8388	0.7927	0.7908	0.8016	0.8377	0.8564
<i>Q_C</i>	0.6132	0.5923	0.6839	0.7107	0.6374	0.6285	0.6642	0.6553	0.6425	0.6982
<i>Q_Y</i>	0.7799	0.7818	<u>0.7964</u>	0.7624	0.7674	0.7483	0.7275	0.7454	0.7673	0.8246
<i>Q_{C-B}</i>	0.6925	0.4957	<u>0.6914</u>	0.5983	0.6503	0.6517	0.6121	0.6093	0.6570	0.6851
<i>R_Q^{F/RS}</i>	0.3511	0.3494	0.3556	0.3426	0.3512	0.3453	0.3498	0.3423	<u>0.3577</u>	0.3602

Table 10: Performance comparison of the proposed method with existing fusion methods for CT-MR pair-5 shown in Fig. 11

Performance Metrics	Fusion Methods									Proposed Method
	Liu et al. [35] (2016)	Liu et al. [37] (2017)	Yin et al. [25] (2018)	Ramlal et al. [13] (2018)	Gansala et al. [15] (2019)	Zhu et al. [10] (2019)	Li et al. [11] (2020)	Tan et al. [14] (2020)	Panigrahy et al. [31] (2020)	
<i>EN</i>	4.5330	4.5116	4.9339	4.9513	5.0078	4.8911	5.1405	5.0030	<u>5.0801</u>	4.9296
<i>SD</i>	61.1048	76.0527	<u>81.4663</u>	81.8346	80.7566	80.1606	80.6482	78.0440	73.4009	78.4415
<i>SF</i>	6.8820	7.0924	7.2984	6.3162	7.5275	7.0613	7.1257	6.9457	<u>7.5004</u>	7.4579
<i>MI</i>	2.9251	2.9345	<u>3.1462</u>	3.1391	3.1125	2.9503	2.9998	3.0736	2.9927	3.3287
<i>Q_{RS/F}</i>	0.5812	<u>0.5905</u>	0.5648	0.5096	0.5605	0.4817	0.5177	0.5487	0.5854	0.6249
<i>Q_{NICE}</i>	0.8967	0.8067	<u>0.8073</u>	0.8073	0.8072	0.8967	0.8969	0.8071	0.8968	0.8079
<i>Q</i>	<u>0.8514</u>	0.8359	0.8370	0.7680	0.8290	0.7851	0.7806	0.8177	0.8249	0.8577
<i>Q_C</i>	<u>0.7259</u>	0.7011	0.5778	0.5854	0.6900	0.5290	0.5523	0.5365	0.6925	0.7482
<i>Q_Y</i>	0.7906	<u>0.8118</u>	0.7845	0.7363	0.7767	0.6922	0.6927	0.7546	0.7667	0.8174
<i>Q_{C-B}</i>	<u>0.6851</u>	0.7088	0.6695	0.5765	0.6328	0.6191	0.5872	0.6206	0.6544	0.6810
<i>R_Q^{F/RS}</i>	0.3500	0.3481	0.3482	0.3336	0.3466	0.3379	0.3413	0.3418	<u>0.3517</u>	0.3576

ranks first in *MI*, *Q_{RS/F}*, *Q_{NICE}*, *Q_C*, *Q_Y* and *R_Q^{F/RS}* which validates the visual assessment of fusion results. For each performance measure, the best performing method is indicated in bold and the second best is presented as underlined. For some image pairs, Li et al. [11] gives higher values of *EN* metric, but the proposed method performs much better in terms of *MI* values alongwith the other quantitative metrics which indicates that the proposed method performs better to reflect the ability for information transfer from source to the fused images. Though Ramlal et al. [13] method gains a higher *SD* values than the proposed method, still, the fused images obtained by the proposed method are visually better alongwith higher edge index *Q_{RS/F}* values. Panigrahy et al. [31] method gains higher *SF* values but results in very lower values of *SD*, *MI* as compared to the proposed

Table 11: Averaged performance analysis of the proposed and other existing fusion methods on CT-MR images (mean \pm standard deviation)

Performance Metrics	Fusion Methods									Proposed Method
	Liu et al. [35] (2016)	Liu et al. [37] (2017)	Yin et al. [25] (2018)	Ramali et al. [13] (2018)	Ganssals et al. [15] (2019)	Zhu et al. [10] (2019)	Li et al. [11] (2020)	Tan et al. [14] (2020)	Panigrahy et al. [31] (2020)	
EN	4.4758 \pm 0.2984	4.7491 \pm 0.3843	4.8155 \pm 0.3749	4.7912 \pm 0.4443	4.9207 \pm 0.3113	4.7056 \pm 0.4059	5.0784 \pm 0.2605	4.9384 \pm 0.2260	4.9726 \pm 0.2531	4.9432 \pm 0.2827
SD	65.265 \pm 3.3174	81.859 \pm 3.6427	86.325 \pm 4.2333	87.272 \pm 4.4150	84.0700 \pm 2.7360	86.1372 \pm 4.682	86.0755 \pm 4.4990	82.5706 \pm 3.806	73.633 \pm 2.5304	83.961 \pm 4.5026
SF	6.5898 \pm 0.5392	6.9634 \pm 0.5554	7.0386 \pm 0.6130	6.2159 \pm 0.6498	7.3420 \pm 0.5657	6.6962 \pm 0.5794	6.8624 \pm 0.6549	6.6710 \pm 0.5877	7.4144 \pm 0.5414	7.1869 \pm 0.6288
MI	2.7499 \pm 0.2017	2.8752 \pm 0.1788	3.0819 \pm 0.1814	3.1004 \pm 0.1537	2.9525 \pm 0.2178	2.9719 \pm 0.1458	3.0052 \pm 0.1631	3.0077 \pm 0.1764	2.8074 \pm 0.2456	3.2243 \pm 0.2582
$Q_{RS/F}$	0.5719 \pm 0.0348	0.5745 \pm 0.0384	0.5345 \pm 0.0511	0.4949 \pm 0.0472	0.5188 \pm 0.0519	0.4805 \pm 0.0554	0.4945 \pm 0.0521	0.5309 \pm 0.0405	0.5637 \pm 0.0405	0.5883 \pm 0.0439
Q_{NICE}	0.8062 \pm 0.0006	0.8066 \pm 0.0007	0.8071 \pm 0.0007	0.8072 \pm 0.0006	0.8068 \pm 0.0008	0.8068 \pm 0.0005	0.8064 \pm 0.0007	0.8069 \pm 0.0006	0.8069 \pm 0.0008	0.8076 \pm 0.0009
Q	0.8251 \pm 0.0324	0.7970 \pm 0.0573	0.8176 \pm 0.0362	0.7731 \pm 0.0361	0.8001 \pm 0.0471	0.7825 \pm 0.0342	0.7609 \pm 0.0293	0.7927 \pm 0.0304	0.8158 \pm 0.0297	0.8258 \pm 0.0283
Q_C	0.6627 \pm 0.0620	0.6593 \pm 0.0659	0.6085 \pm 0.0624	0.6418 \pm 0.0396	0.6594 \pm 0.0511	0.6069 \pm 0.0714	0.6056 \pm 0.0584	0.5687 \pm 0.0652	0.6817 \pm 0.0441	0.7098 \pm 0.0550
Q_Y	0.7384 \pm 0.0629	0.7694 \pm 0.0505	0.7636 \pm 0.0429	0.7382 \pm 0.0378	0.7335 \pm 0.0569	0.7169 \pm 0.0385	0.6981 \pm 0.0331	0.7366 \pm 0.0335	0.7459 \pm 0.0380	0.7786 \pm 0.0537
Q_{CB}	0.6501 \pm 0.0679	0.6256 \pm 0.0935	0.6393 \pm 0.0712	0.5907 \pm 0.0822	0.6100 \pm 0.0672	0.6029 \pm 0.0703	0.5617 \pm 0.0584	0.5959 \pm 0.0466	0.6352 \pm 0.0592	0.6330 \pm 0.0644
$R_Q^{F/RS}$	0.3461 \pm 0.0072	0.3415 \pm 0.0111	0.3421 \pm 0.0092	0.3273 \pm 0.0098	0.3378 \pm 0.0107	0.3300 \pm 0.0113	0.3340 \pm 0.0111	0.3359 \pm 0.0076	0.3458 \pm 0.0086	0.3513 \pm 0.0074

method. The proposed method gains higher EN and MI values than other methods which indicate that our method produces higher information content in the fused images. Moreover, it is capable to reflect sharp edges and visual features very well in the resultant fused images which are indicated by higher SF , $Q_{RS/F}$ and $R_Q^{F/RS}$ values.

To present a concise representation and comparison of the overall fusion performance, another comparison is made and averaged value of performance metrics are presented in Table 11 from which it is observed that the proposed method gets significant better quantitative results in terms of EN , SF , SD , MI , $Q_{RS/F}$, Q_{NICE} , Q , Q_C , Q_Y and $R_Q^{F/RS}$ values. Based on the validation results, the following are the observations,

1. The proposed method yields 17.25%, 12.14%, 4.61%, 3.99%, 9.2%, 8.49%, 7.29%, 7.2% and 14.84% higher values of MI as compared to the aforementioned methods 1-9, respectively which reflect that the fused images obtained by the proposed method contain more visual information compared to the other methods.
2. The proposed fusion methods get 0.08% – 7.68% and 1.20% – 11.53% higher Q and Q_Y respectively which refers to its ability to preserve the salient and complementary information present in source images more efficiently as compared to other fusion methods.
3. The proposed fusion method gets 7.11%, 7.66%, 16.65%, 10.60%, 7.65%, 16.96%, 17.21%, 24.82% and 4.13% higher values of Q_C as compared to the fusion methods 1-9, respectively. Higher Q_C metric value indicates the presence of a higher correlation between the fused and source images.
4. The proposed method gains 2.88%, 2.41%, 10.07%, 18.87%, 13.41%, 22.45%, 18.96%, 10.82% and 4.37% higher $Q_{RS/F}$ values than the fusion method 1-9, respectively. It indicates that the proposed method

outperforms other methods in preserving the structural and edge information present in the source images.

5. The proposed method achieves an average increment of 1.51% – 7.33% for $R_Q^{F/RS}$ metric indicating that the sharp edges are preserved more effectively compared to the other methods.

In addition to this, the proposed method provides significant EN , SD and SF values which indicates that the fused images have better local intensity and contrast and are more visually clear. Therefore, based on the experimental results, it is concluded that the proposed method gives a consistently good performance which is a clear advantage over the other state-of-the-art methods. Also, the proposed fusion method outperforms both in subjective and objective performance leading to give more informative fused images with better preservation of structural and textural information.

5. Conclusions

This paper presents an optimized CT-MR image fusion framework based on two-scale hybrid layer ℓ_1 – ℓ_0 decomposition and BISFNN model using the GWO technique. The detail and base layer obtained from the HLD model provides an effective representation of structural and textural details present in the source images. Fusion rules are framed individually for each layer following the nature of decomposed layers to maximize the preservation of complementary information of CT and MR images. The BISFNN model also helps to extract the features consistent with human visual perception resulting in the fused images with better visual quality. Furthermore, all the free model parameters of HLD and BISFNN are optimized to overcome the manual intervention that also helps to maximize the preservation of sharp edges and enhance the visual quality of the fused images. The superiority of the proposed method is inferred from the experimental results in terms of visual quality and edge preservation. The visual analysis is further validated quantitatively based on different performance metrics which also indicates an ability of the proposed method to preserve more significant information compared to the state-of-the-art methods. Based on results, it is concluded that the proposed fusion method efficiently integrates complementary diagnostic information and is helpful to the radiologist by achieving more factual clinical interpretations.

References

- [1] A. P. James, B. V. Dasarathy, Medical image fusion: A survey of the state of the art, *Information fusion* 19 (2014) 4–19.
- [2] S. Li, X. Kang, L. Fang, J. Hu, H. Yin, Pixel-level image fusion: A survey of the state of the art, *information Fusion* 33 (2017) 100–112.
- [3] S. Li, B. Yang, J. Hu, Performance comparison of different multi-resolution transforms for image fusion, *Information Fusion* 12 (2011) 74–84.
- [4] J. Du, W. Li, B. Xiao, Q. Nawaz, Union laplacian pyramid with multiple features for medical image fusion, *Neurocomputing* 194 (2016) 326–339.
- [5] S. Singh, D. Gupta, R. Anand, V. Kumar, Nonsubsampled shearlet based ct and mr medical image fusion using biologically inspired spiking neural network, *Biomedical Signal Processing and Control* 18 (2015) 91–101.
- [6] R. Srivastava, O. Prakash, A. Khare, Local energy-based multimodal medical image fusion in curvelet domain, *IET computer vision* 10 (2016) 513–527.
- [7] V. Bhateja, H. Patel, A. Krishn, A. Sahu, A. Lay-Ekuakille, Multimodal medical image sensor fusion framework using cascade of wavelet and contourlet transform domains, *IEEE Sensors Journal* 15 (2015) 6783–6790.
- [8] P. Geng, Z. Wang, Z. Zhang, Z. Xiao, Image fusion by pulse couple neural network with shearlet, *Optical Engineering* 51 (2012) 067005.
- [9] S. Das, M. K. Kundu, Nsct-based multimodal medical image fusion using pulse-coupled neural network and modified spatial frequency, *Medical & biological engineering & computing* 50 (2012) 1105–1114.
- [10] Z. Zhu, M. Zheng, G. Qi, D. Wang, Y. Xiang, A phase congruency and local laplacian energy based multi-modality medical image fusion method in nsct domain, *IEEE Access* 7 (2019) 20811–20824.
- [11] X. Li, J. Zhao, A novel multi-modal medical image fusion algorithm, *Journal of Ambient Intelligence and Humanized Computing* (2020) 1–8.

- [12] D. Gupta, Nonsubsampled shearlet domain fusion techniques for ct-mr neurological images using improved biological inspired neural model, *Biocybernetics and Biomedical Engineering* 38 (2018) 262–274.
- [13] S. D. Ramlal, J. Sachdeva, C. K. Ahuja, N. Khandelwal, Multimodal medical image fusion using non-subsampled shearlet transform and pulse coupled neural network incorporated with morphological gradient, *Signal, Image and Video Processing* 12 (2018) 1479–1487.
- [14] W. Tan, P. Tiwari, H. M. Pandey, C. Moreira, A. K. Jaiswal, Multi-modal medical image fusion algorithm in the era of big data, *Neural Computing and Applications* (2020) 1–21.
- [15] P. Ganasala, A. D. Prasad, Medical image fusion based on laws of texture energy measures in stationary wavelet transform domain, *International Journal of Imaging Systems and Technology* (2019).
- [16] S. D. Ramlal, J. Sachdeva, C. K. Ahuja, N. Khandelwal, An improved multimodal medical image fusion scheme based on hybrid combination of nonsubsampled contourlet transform and stationary wavelet transform, *International Journal of Imaging Systems and Technology* 29 (2019) 146–160.
- [17] Z. Liang, J. Xu, D. Zhang, Z. Cao, L. Zhang, A hybrid l1-l0 layer decomposition model for tone mapping, in: *IEEE Conference on Computer Vision and Pattern Recognition, Proceedings of the IEEE conference on computer vision and pattern recognition*, 2018, pp. 4758–4766.
- [18] D. Liu, D. Zhou, R. Nie, R. Hou, Infrared and visible image fusion based on convolutional neural network model and saliency detection via hybrid l0-l1 layer decomposition, *Journal of Electronic Imaging* 27 (2018) 063036.
- [19] E. Daniel, J. Anitha, K. Kamaleshwaran, I. Rani, Optimum spectrum mask based medical image fusion using gray wolf optimization, *Biomedical Signal Processing and Control* 34 (2017) 36–43.
- [20] X. Liu, W. Mei, H. Du, Structure tensor and nonsubsampled shearlet transform based algorithm for ct and mri image fusion, *Neurocomputing* 235 (2017) 131–139.
- [21] X. Xu, Y. Wang, S. Chen, Medical image fusion using discrete fractional wavelet transform, *Biomedical signal processing and control* 27 (2016) 103–111.

- [22] Y. Yang, S. Tong, S. Huang, P. Lin, Log-gabor energy based multimodal medical image fusion in nsct domain, *Computational and mathematical methods in medicine* 2014 (2014).
- [23] S. Singh, R. Anand, Multimodal neurological image fusion based on adaptive biological inspired neural model in nonsubsampling shearlet domain, *International Journal of Imaging Systems and Technology* 29 (2019) 50–64.
- [24] G. Bhatnagar, Q. J. Wu, Z. Liu, A new contrast based multimodal medical image fusion framework, *Neurocomputing* 157 (2015) 143–152.
- [25] M. Yin, X. Liu, Y. Liu, X. Chen, Medical image fusion with parameter-adaptive pulse coupled neural network in nonsubsampling shearlet transform domain, *IEEE Transactions on Instrumentation and Measurement* 68 (2018) 49–64.
- [26] Z. Wang, S. Wang, Y. Zhu, Y. Ma, Review of image fusion based on pulse-coupled neural network, *Archives of Computational Methods in Engineering* 23 (2016) 659–671.
- [27] X. Liu, W. Mei, H. Du, Multimodality medical image fusion algorithm based on gradient minimization smoothing filter and pulse coupled neural network, *Biomedical Signal Processing and Control* 30 (2016) 140–148.
- [28] P. Ganasala, V. Kumar, Feature-motivated simplified adaptive pcnn-based medical image fusion algorithm in nsst domain, *Journal of Digital Imaging* 29 (2016) 73–85.
- [29] L. Tang, C. Tian, K. Xu, Igm-based perceptual multimodal medical image fusion using free energy motivated adaptive pcnn, *International Journal of Imaging Systems and Technology* 28 (2018) 99–105.
- [30] L. Tang, J. Qian, L. Li, J. Hu, X. Wu, Multimodal medical image fusion based on discrete t chebichef moments and pulse coupled neural network, *International Journal of Imaging Systems and Technology* 27 (2017) 57–65.
- [31] C. Panigrahy, A. Seal, N. K. Mahato, Mri and spect image fusion using a weighted parameter adaptive dual channel pcnn, *IEEE Signal Processing Letters* 27 (2020) 690–694.

- [32] X. Xu, G. Wang, S. Ding, Y. Cheng, X. Wang, Pulse-coupled neural networks and parameter optimization methods, *Neural Computing and Applications* 28 (2017) 671–681.
- [33] Y. Liu, X. Chen, R. K. Ward, Z. J. Wang, Medical image fusion via convolutional sparsity based morphological component analysis, *IEEE Signal Processing Letters* 26 (2019) 485–489.
- [34] S. Singh, R. Anand, Multimodal medical image sensor fusion model using sparse k-svd dictionary learning in nonsubsamped shearlet domain, *IEEE Transactions on Instrumentation and Measurement* 69 (2020) 593–607.
- [35] Y. Liu, X. Chen, R. K. Ward, Z. J. Wang, Image fusion with convolutional sparse representation, *IEEE signal processing letters* 23 (2016) 1882–1886.
- [36] Q. Zhang, Y. Liu, R. S. Blum, J. Han, D. Tao, Sparse representation based multi-sensor image fusion for multi-focus and multi-modality images: A review, *Information Fusion* 40 (2018) 57–75.
- [37] Y. Liu, X. Chen, J. Cheng, H. Peng, A medical image fusion method based on convolutional neural networks, in: *20th International Conference on Information Fusion (Fusion)*, 20th International Conference on Information Fusion, 2017, pp. 1–7.
- [38] H. Hermessi, O. Mourali, E. Zagrouba, Convolutional neural network-based multimodal image fusion via similarity learning in the shearlet domain, *Neural Computing and Applications* 30 (2018) 2029–2045.
- [39] C. Xydeas, , V. Petrovic, Objective image fusion performance measure, *Electronics letters* 36 (2000) 308–309.
- [40] J. L. Johnson, Pulse-coupled neural networks, in: *Adaptive Computing: Mathematics, Electronics, and Optics: A Critical Review*, volume 10277, International Society for Optics and Photonics, 1994, p. 1027705.
- [41] G. Qu, D. Zhang, P. Yan, Information measure for performance of image fusion, *Electronics letters* 38 (2002) 313–315.
- [42] Q. Wang, Y. Shen, Performances evaluation of image fusion techniques based on nonlinear correlation measurement, in: *21st IEEE Instrumentation and Measurement Technology Conference*, volume 1, Proceedings

of the 21st IEEE Instrumentation and Measurement Technology Conference, 2004, pp. 472–475.

- [43] G. Piella, H. Heijmans, A new quality metric for image fusion, in: International Conference on Image Processing, volume 3, Proceedings 2003 International Conference on Image Processing, 2003, pp. III–173.
- [44] N. Cvejic, A. Loza, D. Bull, N. Canagarajah, A similarity metric for assessment of image fusion algorithms, International journal of signal processing 2 (2005) 178–182.
- [45] C. Yang, J.-Q. Zhang, X.-R. Wang, X. Liu, A novel similarity based quality metric for image fusion, Information Fusion 9 (2008) 156–160.
- [46] Y. Chen, R. S. Blum, A new automated quality assessment algorithm for image fusion, Image and vision computing 27 (2009) 1421–1432.
- [47] A. Sengupta, A. Seal, C. Panigrahy, O. Krejcar, A. Yazidi, Edge information based image fusion metrics using fractional order differentiation and sigmoidal functions, IEEE Access 8 (2020) 88385–88398.
- [48] X. Xinzhen, D. Shifei, S. Zhongzhi, Z. Hong, Z. Zuopeng, Particle swarm optimization for automatic parameters determination of pulse coupled neural network, J Computers 6 (2011) 1546–1553.
- [49] W. Gómez-Flores, J. Hernández-López, Automatic adjustment of the pulse-coupled neural network hyperparameters based on differential evolution and cluster validity index for image segmentation, Applied Soft Computing (2019) 105547.